Journal of Power Sources 195 (2010) 5025–5031

Contents lists available at ScienceDirect

Journal of Power Sources

journal homepage: www.elsevier.com/locate/jpowsour

Electrodeposited MnO*x*/carbon nanofiber composites for use as anode materials in rechargeable lithium-ion batteries

Zhan Lin [1], Liwen Ji [1], Mariah D. Woodroof, Xiangwu Zhang*

Fiber and Polymer Science Program, Department of Textile Engineering, Chemistry and Science, North Carolina State University, 2401 Research Drive, Raleigh, NC 27695-8301, USA

ARTICLE INFO

Article history:
Received 25 December 2009
Received in revised form 29 January 2010
Accepted 1 February 2010
Available online 6 February 2010

Keywords:
Electrospinning
Electrodeposition
MnO*x* nanoparticles
Carbon nanofibers
Lithium-ion batteries

ABSTRACT

Carbon nanofiber-supported MnO*x* composites were prepared by electrodepositing MnO*x* nanoparticles directly onto electrospun carbon nanofibers. The morphology and size of MnO*x* nanoparticles were controlled by the surface treatment of carbon nanofibers and the electrodeposition duration time. SEM, TEM/EDS, elemental analysis, and XRD were used to study the morphology and composition of MnO*x* on the nanofibers. The resultant MnO*x*/carbon nanofiber composites were used directly as the anode material in lithium half cells and their electrochemical performance was characterized. Results show that MnO*x*/carbon nanofiber composites prepared by different deposition durations have high reversible capacity, good capacity retention, and excellent structural integrity during cycling.

1. Introduction

Stimulated by the fossil fuel depletions, energy crisis, and environmental pollution throughout the world, the pursuit of alternative energy conversion and storage systems has gained more and more attention in recent decades [1–8]. Among various energy storage systems, rechargeable lithium-ion batteries (LIBs) have become a primary research focus because lithium chemistry has many advantages, such as a high electrode potential, high energy density, and low gravimetric density [9,10]. Since the first introduction of LIBs into the market in 1991, graphite has been widely used as the anode material due to its low cost, non-toxicity, and good safety by overcoming the production of dendrites [11]. However, the theoretical capacity of the graphite is limited to 372 mAh g^{-1} [12–14].

Novel carbon nanomaterials, such as carbon nanotubes (CNTs), carbon nanofibers (CNFs), and graphene, have been considered as promising candidates for anode materials in LIBs [15–22]. For example, Kim et al. reported the fabrication of electrospun CNFs, which has a capacity of 450 mAh g^{-1} [23]; however, this capacity is still relatively low. One approach to improve the electrochemical performance of carbon nanomaterials is to incorporate them with higher capacity anode materials.

Until now, various transition metal oxides, such as tin-, iron-, and copper-based oxides, have been widely investigated as the anode materials in LIBs, since they possess the good properties of high theoretical capacity, environmental benignity, safety, and low cost [24–31]. Among various transition metal oxides, manganese oxides (MnO*x*) have been reported as both cathode and anode materials in LIBs with high performance. The capacities of manganese oxides as anode materials are between 500 and 1000 mAh g^{-1} [32–34], depending on their chemical and physical structures [33,35–37]. However, the poor electronic conductivity and large volume change during repeated lithium insertion/extraction are major problems for using MnO*x* as anode materials in practical LIBs. Extensive research has been devoted to solve these problems by preparing composites, coating carbons, and adding electronically conductive materials [38–41].

In order to fabricate the anode materials with improved electronic conductivity and higher capacity in LIBs, transitional metal oxides/carbon-based nanofiber composites with improved electrochemical performance need to be synthesized. In this paper, we demonstrate the preparation of MnO*x*/carbon nanofiber composites (MnO*x*/CNFs) through the electrodeposition of MnO*x* nanoparticles onto CNFs and their enhanced electrochemical performance as the anode material in lithium half cells.

2. Experimental

2.1. Chemicals and reagents

Polyacrylonitrile (PAN), N,N-dimethylformamide (DMF), manganese acetate [$Mn(CH_3COO)_2$], and sodium sulfate (Na_2SO_4) were

* Corresponding author. Tel.: +1 919 515 6547; fax: +1 919 515 6532.
E-mail address: xiangwu_zhang@ncsu.edu (X. Zhang).
[1] These authors contributed equally to this work.

0378-7753/$ – see front matter © 2010 Elsevier B.V. All rights reserved.
doi:10.1016/j.jpowsour.2010.02.004

purchased from Sigma–Aldrich and were used without further purification. Deionized water was used throughout.

2.2. Synthesis of CNFs

A DMF solution of 8 wt% PAN was prepared at 60 °C, with mechanical stirring for 3 h. The electrospinning was conducted using a Gamma ES40P-20W/DAM variable high voltage power supply under a voltage of 15 kV. Under high voltage, a polymer jet was ejected and accelerated toward the nanofiber collector, during which the solvent was rapidly evaporated. The electrospun PAN fibers were collected on an aluminum foil placed on the collector. These PAN nanofibers were first stabilized in an air atmosphere at 280 °C for 6 h with a heating rate of 5 °C min^{-1}, and then carbonized at 600 °C for 8 h in argon atmosphere with a heating rate of 2 °C min^{-1}. The resultant CNFs were used as the working electrode in the electrodeposition of MnO*x* nanoparticles.

2.3. Electrodeposition of MnOx onto CNFs

The electrodeposition of MnO*x* particles onto CNFs were performed on an AQ4 Gamry Reference 600 electrochemical workstation at 25 °C using a three-electrode cell, which consisted of a working electrode (CNFs), a counter electrode (Pt wire), and a reference electrode (Ag/AgCl/4.0 M KCl). Argon was used to bubble the solution for at least 30 min before the electrodeposition, and then was used continually to protect the experiment environment. Before the electrodeposition, CNFs were cycled and oxidized in 1 M H_2SO_4 solution between −0.7 and 1.2 V for 100 cycles at 50 mV s^{-1}, and then used as the working electrode for the deposition of MnO*x* nanoparticles by applying a potential of −0.2 V (*vs.* Ag/AgCl/4.0 M KCl) with different deposition durations in a 0.1 M $Mn(CH_3COO)_2$ + 0.1 M Na_2SO_4 solution. After the electrodeposition, MnO*x*/CNFs were calcinated at 600 °C for 1 h in Argon and used as the anode materials in LIBs.

2.4. Characterization of MnOx/CNFs

X-ray diffraction (XRD) analysis was performed with a Philips XLF ATPS XRD 100 diffractometer using CuKα radiation (λ = 1.5405 Å). The operating voltage and current were 45 kV and 40 mA, respectively. Elemental analysis was conducted by using a CE440 Elemental Analyzer.

The structure of CNFs and MnO*x*/CNFs, which were deposited onto 200 mesh carbon-coated Cu grids, was evaluated using a

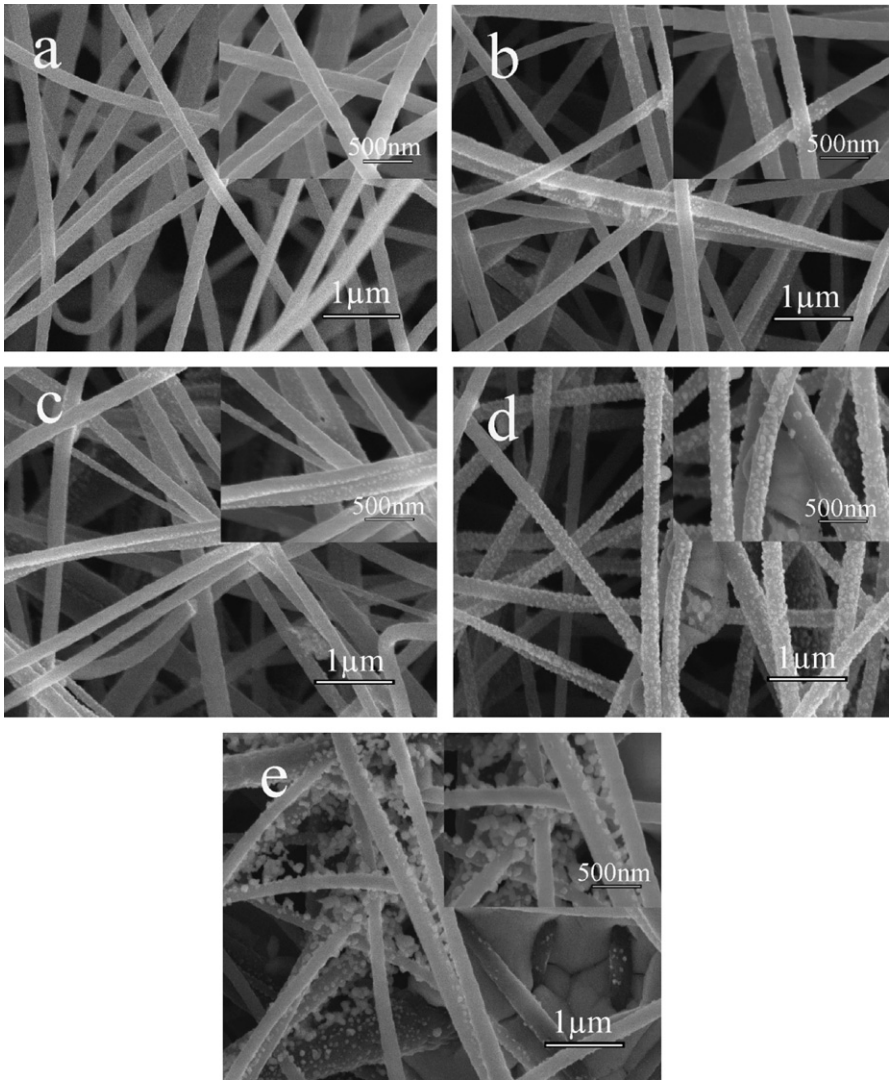

Fig. 1. SEM images of CNFs (a) and MnO*x*/CNFs prepared with different deposition durations of 2.5 (b), 5 (c), 10 (d), and 20 (e) h. The insets of images (a)–(e) show CNFs and MnO*x*/CNFs with higher magnification.

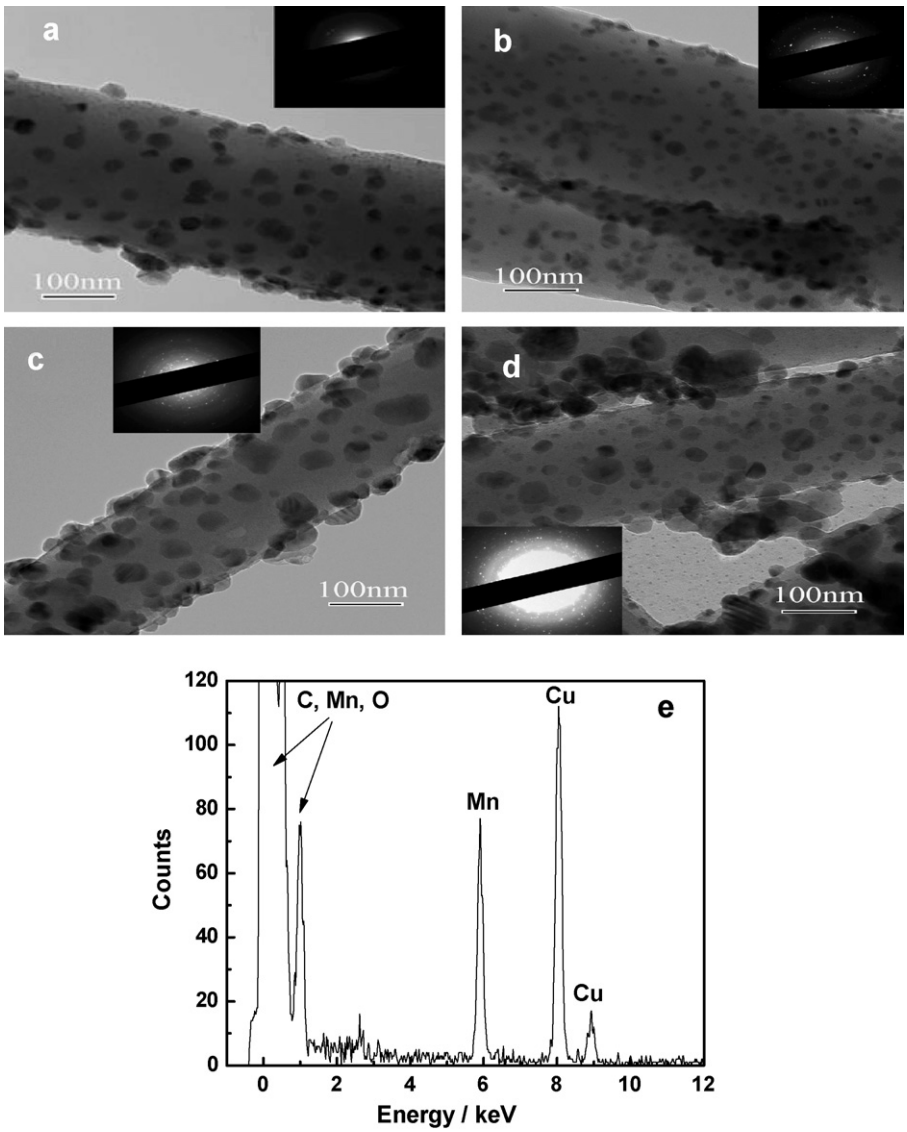

Fig. 2. TEM images of MnO*x*/CNFs prepared with different deposition durations of 2.5 (a), 5 (b), 10 (c), and 20 (d) h, respectively; and EDS spectrum (e) of MnO*x*/CNFs with 10 h deposition. The insets in (a), (b), (c), and (d) show the electron diffraction patterns.

Hitachi HF-2000 TEM at 200 kV. These CNFs and MnO*x*/CNFs were also examined using a JEOL JSM-6360LV FESEM at 15 kV. The diameters of MnO*x* nanoparticles were determined by measuring 81 randomly selected particles using an ImageJ software package.

2.5. Electrochemical properties of MnOx/CNFs

Coin-type cells 2032 were used to evaluate the electrochemical performance of MnO*x*/CNFs. MnO*x*/CNFs attached onto copper foil (Lyon industries), lithium ribbon (Aldrich), and Separion S240 P25 (Degussa) were directly used as the working electrode, counter electrode, and separator, respectively. The electrolyte lithium hexafluorophosphate ($LiPF_6$, 1 M) was dissolved in 1/1 (v/v) ethylene carbonate (EC)/ethyl methyl carbonate (EMC). Charge and discharge were carried out using an Arbin battery cycler at various current densities between cut-off potentials 0.01 and 2.8 V. Both charge and discharge capacities were calculated based on the total weight of MnO*x*/CNFs.

3. Results and discussion

3.1. SEM images of MnOx/CNFs

Before the electrodeposition, CNFs were used as the working electrode and were cycled in 1.0 M H_2SO_4 to carry out the surface oxidation. During that process, various surface functional groups, such as quinoid (=O), hydroxy (–OH), and carboxyl (–COOH), were produced, which can supply defect sites for MnO*x* nanoparticle deposition [42]. After the surface oxidation, MnO*x* nanoparticles were electrodeposited onto the CNF surface. Fig. 1 shows SEM images of CNFs and MnO*x*/CNFs with different deposition durations. It is seen that the surface of CNFs is smooth and there are no particles found (Fig. 1a). When the deposition time is 2.5 h, only a few MnO*x* nanoparticles are found on the surface of CNFs due to the relatively low MnO*x* loading. When the deposition durations are beyond 2.5 h, *e.g.* 5 and 10 h, more and more MnO*x* nanoparticles are evenly distributed on the surface of CNFs. However, when the deposition time is 20 h, there are MnO*x* nanoparticle aggregates found. Moreover, the elemental analysis was used to calculate

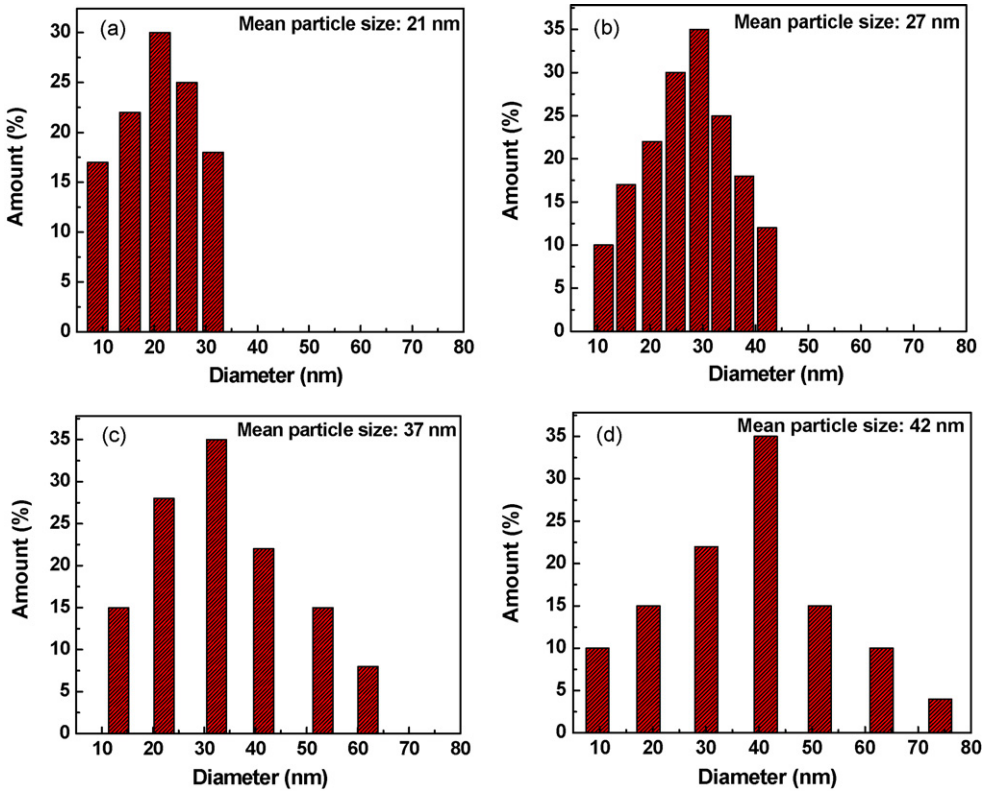

Fig. 3. Diameter distributions of MnO*x* particles in MnO*x*/CNFs prepared with different deposition durations: 2.5 (a), 5 (b), 10 (c), and 20 (d) h.

the deposition amount of MnO*x* nanoparticles in MnO*x*/CNFs, and it is found that the deposition amount is around 0.04, 0.07, 0.15, and 0.25 g Mn per g CNF for the deposition durations of 2.5, 5, 10, and 20 h, respectively. The application of a longer deposition time typically results in higher MnO*x* nanoparticle loading, which can be seen in the insets of SEM images with higher magnification in Fig. 1.

3.2. TEM images of MnOx/CNFs

Fig. 2 shows TEM images of MnO*x*/CNFs with different deposition durations. In Fig. 2a, it is seen that MnO*x* nanoparticles are found on the surface of CNFs after 2.5 h electrodeposition, and the average diameter of MnO*x* nanoparticles is around 21 nm (Fig. 3a). When the deposition duration increases to 5 and 10 h, more and more MnO*x* nanoparticles are evenly distributed on the surface of CNFs, and their average diameters increase to 27 and 37 nm, respectively (Fig. 3b and c). Longer deposition time leads to higher particle loading without increasing the quantity of nuclei. The higher particle loading (*i.e.*, MnO*x* loading), in turn, increases the MnO*x* nanoparticle size. However, when the deposition time is 20 h, there are also some aggregates found. The insets of TEM images show the electron diffraction patterns of MnO*x*/CNFs, which demonstrate the formation of MnO*x* crystal structure on the surface of CNFs. Fig. 2e shows the energy dispersive X-ray spectroscopy (EDS) of MnO*x*/CNFs prepared with 10 h deposition. The EDS curve also confirms the presence of MnO*x* particles on the surface of CNFs. The Cu peak in Fig. 2e comes from the TEM grid background.

3.3. XRD patterns of CNFs and MnOx/CNFs

X-ray diffraction (XRD) patterns obtained from CNFs and MnO*x*/CNFs are illustrated in Fig. 4. The diffraction peak of CNFs at around 25° results from the diffraction of the (0 0 2) plane of graphite layers. The XRD pattern of MnO*x*/CNFs presents typical diffraction peaks of MnO*x*, which are 37.9° (2 0 0) and 58.2° (2 2 0) for MnO, 21.9° (1 1 1), 26.7° (2 0 2), and 33.8° (2 2 1) for Mn_2O_3, and 25.8° (2 1 1), 28.5° (1 1 2), and 31.8° (3 1 1) for Mn_3O_4, respectively. All these peaks confirm the formation of MnO*x* crystals on the surface of CNFs.

3.4. Electrochemical performance of MnOx/CNFs

In order to study the electrochemical performance, the MnO*x*/CNFs prepared with 10 h deposition duration were charged/discharged between cut-off potentials 0.01 and 2.8 V

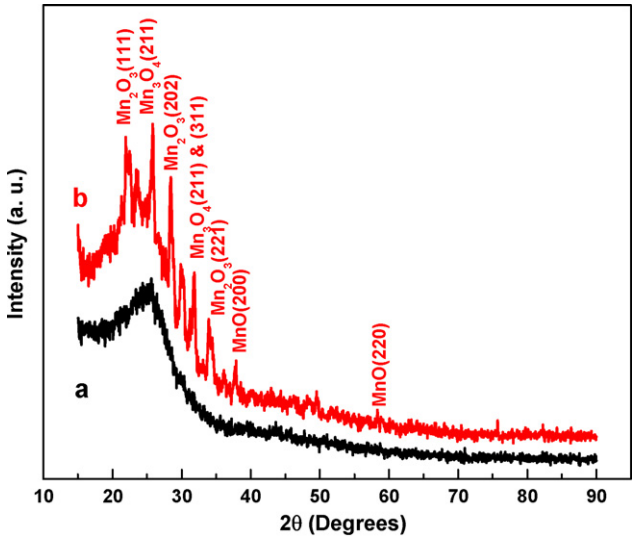

Fig. 4. XRD patterns of CNFs (a) and MnO*x*/CNFs (b). Deposition time: 10 h.

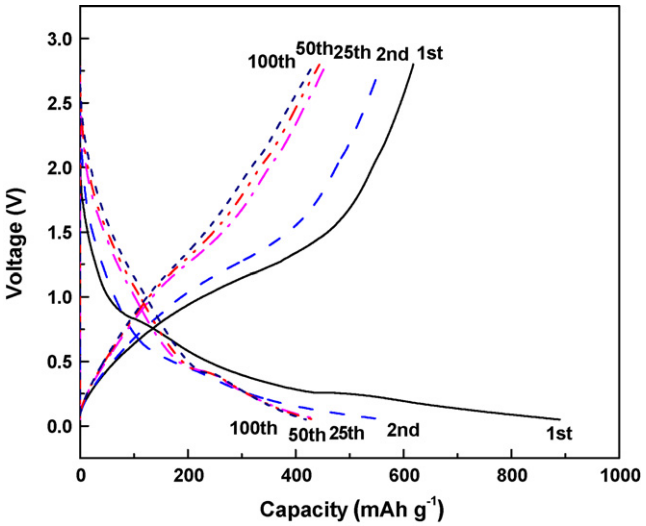

Fig. 5. Charge–discharge curves of MnO*x*/CNF composite anode at a constant current density 50 mA g^{-1}. Deposition time: 10 h.

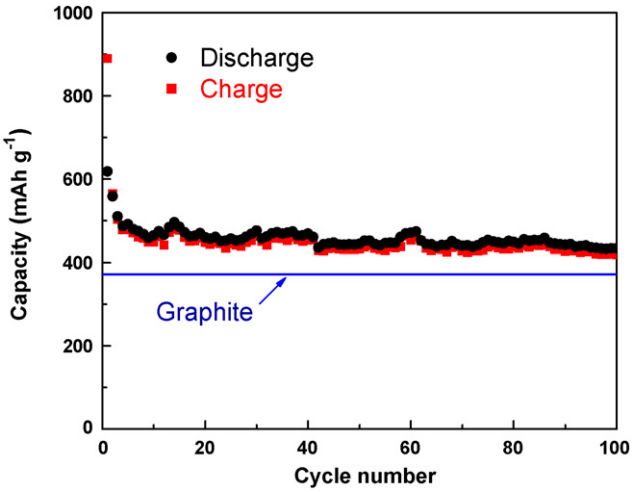

Fig. 6. Cycling performance of MnO*x*/CNF composite anode at a constant current density 50 mA g^{-1}. Deposition time: 10 h.

at a constant current density of 50 mA g^{-1}, and the results are shown in Fig. 5. During the first charge (lithium insertion), three voltage ranges, *e.g.*, 2.8–0.8, 0.8–0.3 and 0.3–0.01 V *vs.* Li^+/Li, can be found. The first range can be attributed to the decomposition of the electrolyte and the formation of solid electrolyte interphase (SEI) film and other inactive materials [43–46]. The second and third one is related to the insertion of lithium into the MnO*x*/CNF composite, and the possible reaction mechanism of manganese oxides with lithium has been proposed as the following:

$$MnOx + 2xLi \leftrightarrow xLi_2O + Mn \quad (1)$$

In the first voltage range of 2.8–0.8 V, the charge capacity is irreversible, but the capacities of the second (0.8–0.3 V) and third (0.3–0.01 V) potential ranges are reversible if the anode material can withstand the large volume change during charge/discharge [43–46]. From the first cycle shown in Fig. 5, it can also be seen that MnO*x*/CNFs show charge and discharge capacities of about 890 and 618 mAh g^{-1}, respectively, corresponding to a coulombic efficiency (discharge capacity/charge capacity) of 69%. However, after the 1st cycle, the coulombic efficiency of MnO*x*/CNFs remains at nearly 100%. Moreover, compared to the charge/discharge capacities of CNFs reported in our previous work (*e.g.*, in the 2nd cycle, the discharge capacity of CNFs is 493 mAh g^{-1} at 50 mA g^{-1}) [47], the charge/discharge capacities of MnO*x*/CNFs are higher (*e.g.*, the discharge capacity is 558 mAh g^{-1} in the 2nd cycle), which should be due to the higher capacity of MnO*x*.

3.5. Cycling performance of MnOx/CNFs

The cycling performance of MnO*x*/CNFs (deposition time = 10 h) and the theoretical value of graphite, currently the most commonly used commercial anode material, are compared in Fig. 6. The reversible capacity of MnO*x*/CNFs at the second cycle is about 558 mAh g^{-1}, which indicates about 90% retention of the initial value (618 mAh g^{-1}) at the first cycle. Moreover, the reversible capacities of MnO*x*/CNFs are about 474, 476, and 444 mAh g^{-1} for the tenth, thirtieth, and fiftieth cycle (76, 77, and 72% retentions of the initial value), respectively. Moreover, after 100 cycles, the reversible capacity of these MnO*x*/CNFs is still kept at 433 mAh g^{-1} (70% retention of the initial value), which indicates a relatively slow fading in the reversible capacity. Therefore, the reversible capacity of MnO*x*/CNFs is much larger than the theoretical capacity of graphite (372 mAh g^{-1}). The relatively high capacity and good cycling behavior of MnO*x*/CNFs can be ascribed to their unique composite structure, such as the good electric conductivity of CNF matrix, the relatively high Li storage in MnO*x*, and the buffer effects of the CNF matrix during lithium insertion/extraction.

3.6. Rate capacities of MnOx/CNFs

Generally, the capacities of LIB anodes decrease with increase in current density, which is a big challenge in commercially available graphite-based anode materials since their rate capacities are relatively low [48,49]. The discharge capacities of MnO*x*/CNFs (deposition time = 10 h) at different current densities, *i.e.*, 50, 100, 200, 300, and 500 mA g^{-1}, are shown in Fig. 7. In the 2nd cycle, when the current density is 100 mA g^{-1}, MnO*x*/CNFs show relatively little degradation in capacity compared with that in 50 mA g^{-1}. Although there is a relatively high capacity decrease when the current density is 200 mA g^{-1}, the capacity almost levels off when the current density increases to 300 mA g^{-1}. However, the capacity decreases again when the current density is 500 mA g^{-1}. In the 50th cycle, when the current density is 200 mA g^{-1}, the capacity of MnO*x*/CNFs is about 400 mAh g^{-1}, which is comparable to those at 50 and 100 mA g^{-1}, respectively. When the current density continues to increase to

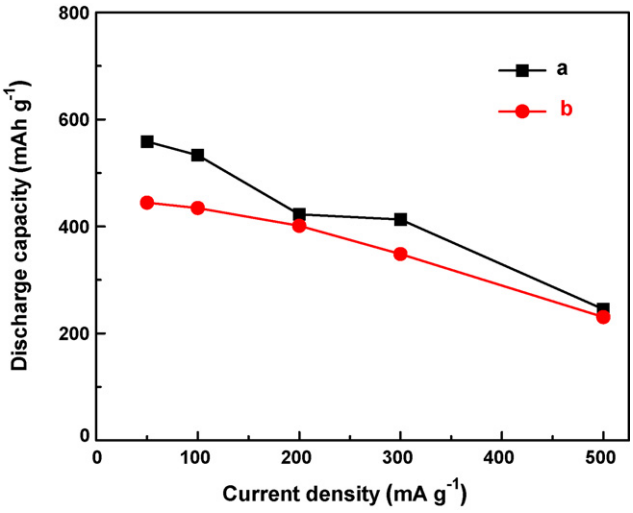

Fig. 7. Rate capability of MnO*x*/CNF composite anode in the 2nd (a) and 50th (b) cycles. Deposition time: 10 h.

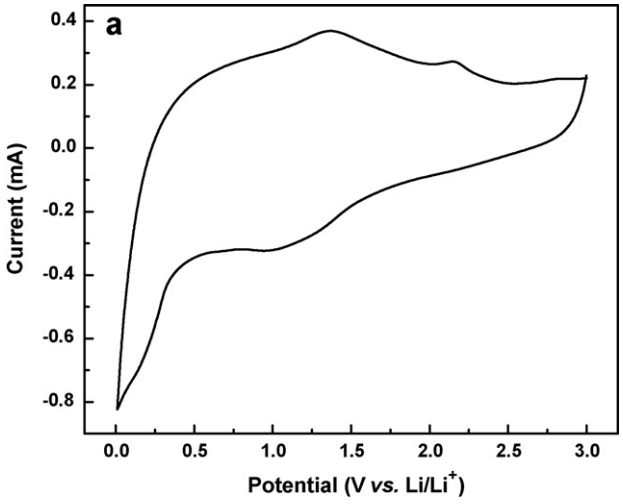

Fig. 8. The cyclic voltammogram at a scan rate of 0.1 mV s^{-1} in cut-off potentials of 0.01–2.8 V (a) and SEM images (b) of MnO*x*/CNFs after 100 charge/discharge cycles at a constant current density of 50 mA g^{-1}. Deposition time: 10 h. The inset of the SEM image shows MnO*x*/CNFs with higher magnification.

300 and 500 mA g^{-1}, the capacity of MnO*x*/CNFs decreases. However, when the current density is 500 mA g^{-1}, the capacities of MnO*x*/CNFs at the 2nd and 50th cycles are almost the same.

3.7. Integrity of MnOx/CNFs

In order to understand the influence of charge/discharge process on the structural integrity of MnO*x*/CNFs, cyclic voltammogram (CV) and SEM images were taken after 100 charge/discharge cycles at a constant current density of 50 mA g^{-1}. Fig. 8a shows the CV of MnO*x*/CNFs with 10 h deposition at a scan rate of 0.1 mV s^{-1} in cut-off potentials of 0.01–2.8 V. It is seen that a pronounced broad cathodic peak appeared at around 0.95 V and two fairly broad anodic peaks were present at 1.37 and 2.12 V, respectively. These peaks should be attributed to the reversible electrochemical oxidation (Li extraction) and reduction (Li insertion) of MnO*x* with lithium, which are caused by phase transitions during lithium insertion/extraction [36,50]. The good reversibility of nanofiber composites could be the result of unique MnO*x*/CNF structure, *i.e.*, a uniform distribution of MnO*x* nanoparticles on the surface of CNFs.

Fig. 8b shows SEM images of MnO*x*/CNFs with 10 h deposition after 100 charge/discharge cycles at a constant current density of 50 mA g^{-1}. It is seen that all CNFs still exhibit a relatively similar morphology after 100 cycles when compared with MnO*x*/CNFs before cycling (Fig. 1), which indicates that the structural integrity of CNFs is preserved during charge/discharge [51,52]. These results

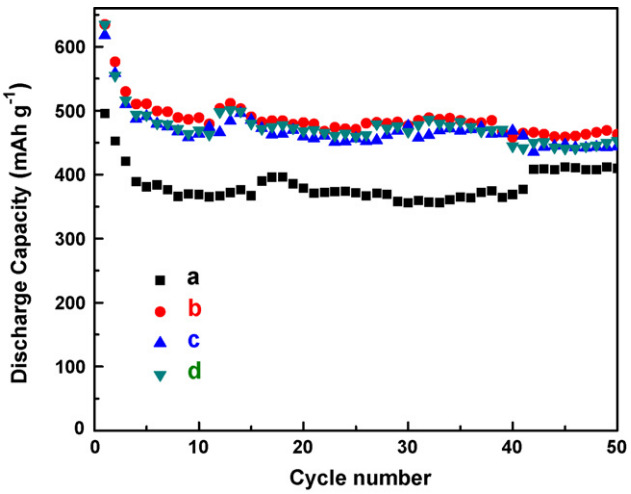

Fig. 9. Cycling performance of MnO*x*/CNFs prepared with different electrodeposition durations: 2.5 (a), 5 (b), 10 (c), and 20 (d) h.

also reveal that CNFs can help LIB anodes to withstand the large volume expansion and shrinkage during lithium insertion and extraction processes. However, the MnO*x* nanoparticles are hard to be found after cycling (Fig. 8b), which may be due to the formation of the SEI layer since the element Mn can still be observed on the surface of CNFs based on SEM/EDS analysis (not shown in the figure).

3.8. Performance optimization of MnOx/CNFs

In order to optimize the performance of MnO*x*/CNF composite anodes, the cycling performance of MnO*x*/CNFs prepared with different electrodeposition durations are shown in Fig. 9. When the deposition time is 2.5 h, the discharge capacity of MnO*x*/CNFs is relatively low and almost keeps at around 370 mAh g^{-1}, which should be due to the relatively low loading of MnO*x* nanoparticles on the surface of CNFs. When the electrodeposition time is 5 h, the discharge capacity of MnO*x*/CNFs reaches at a maximum; however, when the deposition time is 10 h, the discharge capacity decreases slightly. When the deposition time increases from 2.5 to 5 h, the increase of the discharge capacity is due to the increased amount of available MnO*x* particles. When the deposition time is beyond 10 h, the capacity decreases although much more MnO*x* nanoparticles are available, which may be due to the aggregates of MnO*x* nanoparticles on the surface of CNFs.

4. Conclusions

MnO*x*/CNFs have been prepared by electrodepositing MnO*x* nanoparticles onto electrospun CNFs under the potential −0.2 V. Particles with well-defined morphology and size were obtained by controlling the electrodeposition time. The deposition time can also be used to control the MnO*x* loading and the electrochemical performance. The resultant MnO*x*/CNF composites possess high reversible capacity, good capacity retention, and great integrity after cycling when tested as anodes in LIBs. The electrochemical performance optimization of MnO*x*/CNF composites has also been conducted. The results show that the MnO*x*/CNF composite with a suitable deposition time (such as 5 h) has the best electrochemical performance in terms of the discharge capacity. To sum up, the electrochemical deposition of MnO*x* nanoparticles onto CNFs has provided an alternative method to obtain good anode materials in LIBs, which make such composites possible as the anodes in LIBs. However, further improvements are needed to optimize

the SEI formation, increase the volumetric capacity, and reduce the energy consumption before these composites can be used in practical batteries.

Acknowledgements

This work was supported by the Department of Energy (DE-EE0001177), the National Textile Center (ITA-08-07400), U.S. National Science Foundation (0833837), and ACS Petroleum Research Fund (47863-G10).

References

[1] M. Kundu, S. Mahanty, R.N. Basu, Electrochem. Commun. 11 (2009) 1389–1392.
[2] R. Malini, U. Uma, T. Sheela, M. Ganesan, N.G. Renganathan, Ionics 15 (2009) 301–307.
[3] J.F. Shen, Y.Z. Hua, C. Li, C. Qin, M.X. Ye, Electrochim. Acta 53 (2008) 7276–7280.
[4] E.E. Switzer, A.K. Datye, P. Atanassov, Top. Catal. 46 (2007) 334–338.
[5] Z.C. Tang, G.X. Lu, Prog. Chem. 19 (2007) 1301–1312.
[6] J.A. Tian, G.Q. Sun, L.H. Jiang, S.Y. Yan, Q. Mao, Q. Xin, Electrochem. Commun. 9 (2007) 563–568.
[7] Y.D. Wang, I. Djerdj, B. Smarsly, M. Antonietti, Chem. Mater. 21 (2009) 3202–3209.
[8] J.P. Yu, X.H. Hu, H. Zhan, Y.H. Zhou, J. Power Sources 189 (2009) 697–701.
[9] T.F. Yi, J. Shu, Y.R. Zhu, X.D. Zhu, C.B. Yue, A.N. Zhou, R.S. Zhu, Electrochim. Acta 54 (2009) 7464–7470.
[10] H. Wolf, Z. Pajkic, T. Gerdes, M. Willert-Porada, J. Power Sources 190 (2009) 157–161.
[11] M. Wakihara, Mater. Sci. Eng. R33 (2001) 109–134.
[12] L.J. Fu, H. Liu, C. Li, Y.P. Wu, E. Rahm, R. Holze, H.Q. Wu, Solid State Sci. 8 (2006) 113–128.
[13] T. Nakajima, J. Fluorine Chem. 105 (2000) 229–238.
[14] M. Yoshio, H.Y. Wang, K. Fukuda, Angew. Chem. Int. Ed. 42 (2003) 4203–4206.
[15] P. Guo, H.H. Song, X.H. Chen, Electrochem. Commun. 11 (2009) 1320–1324.
[16] H. Huang, W.K. Zhang, X.P. Gan, C. Wang, L. Zhang, Mater. Lett. 61 (2007) 296–299.
[17] T.I.T. Kudin, N.F.A. Zainal, A.M.M. Ali, S. Abdullah, M. Rusop, M.A. Sulaiman, M.Z.A. Yahya, Mater. Res. Innov. 13 (2009) 269–271.
[18] J. Shu, H. Li, R.Z. Yang, Y. Shi, X.J. Huang, Electrochem. Commun. 8 (2006) 51–54.
[19] G.X. Wang, X.P. Shen, J. Yao, J. Park, Carbon 47 (2009) 2049–2053.
[20] J.Y. Yan, H.H. Song, S.B. Yang, J.D. Yan, X.H. Chen, Electrochim. Acta 53 (2008) 6351–6355.
[21] J.T. Yin, M. Wada, Y. Kitano, S. Tanase, O. Kajita, T. Sakai, J. Electrochem. Soc. 152 (2005) A1341–A1346.
[22] E. Yoo, J. Kim, E. Hosono, H. Zhou, T. Kudo, I. Honma, Nano Lett. 8 (2008) 2277–2282.
[23] C. Kim, K.S. Yang, M. Kojima, K. Yoshida, Y.J. Kim, Y.A. Kim, M. Endo, Adv. Funct. Mater. 16 (2006) 2393–2397.
[24] S.K. Chang, H.J. Kim, S.T. Hong, J. Power Sources 119 (2003) 69–75.
[25] K.B. Wan, S.F.Y. Li, Z.Q. Gao, K.S. Siow, J. Power Sources 75 (1998) 9–12.
[26] G.X. Wang, X.P. Shen, J.N. Yao, D. Wexler, J. Ahn, Electrochem. Commun. 11 (2009) 546–549.
[27] S.Q. Wang, J.Y. Zhang, N. Ding, C.H. Chen, Scripta Mater. 60 (2009) 1117–1120.
[28] J. Xiao, N.A. Chernova, M.S. Whittingham, Chem. Mater. 20 (2008) 7454–7464.
[29] H. Yoshizawa, T. Ohzuku, J. Power Sources 174 (2007) 813–817.
[30] Y. Yu, C.H. Chen, Y. Shi, Adv. Mater. 21 (2009) 3541–13541.
[31] Y.L. Zhang, Y. Liu, M.L. Liu, Chem. Mater. 18 (2006) 4643–4646.
[32] K. Zhong, X. Xia, B. Zhang, H. Li, Z. Wang, L. Chen, J. Power Sources 195 (2009) 3300–3308.
[33] Q. Fan, M.S. Whittingham, Electrochem. Solid-State Lett. 10 (2007) A48–A51.
[34] M.M. Thackeray, Prog. Solid State Chem. 25 (1997) 1–71.
[35] M.M. Thackeray, C.S. Johnson, J.T. Vaughey, N. Li, S.A. Hackney, J. Mater. Chem. 15 (2005) 2257–2267.
[36] M.S. Wu, P.C.J. Chiang, Electrochem. Commun. 8 (2006) 383–388.
[37] Y. Yang, D. Shu, H. Yu, X. Xia, Z.G. Lin, J. Power Sources 65 (1997) 227–230.
[38] C. Arbizzani, A. Balducci, M. Mastragostino, M. Rossi, F. Soavi, J. Electroanal. Chem. 553 (2003) 125–133.
[39] K. Ariyoshi, E. Iwata, M. Kuniyoshi, H. Wakabayashi, T. Ohzuku, Electrochem. Solid-State Lett. 9 (2006) A557–A560.
[40] H. Kawaoka, M. Hibino, H.S. Zhou, I. Honma, J. Electrochem. Soc. 152 (2005) A1217–A1220.
[41] Z.Y. Tang, N. Zhang, X.H. Lu, Q.H. Huang, J. Rare Earths 23 (2005) 120–123.
[42] A. Rasheed, J.Y. Howe, M.D. Dadmun, P.F. Britt, Carbon 45 (2007) 1072–1080.
[43] R. Demir-Cakan, Y.S. Hu, M. Antonietti, J. Maier, M.M. Titirici, Chem. Mater. 20 (2008) 1227–1229.
[44] Y.S. Hu, R. Demir-Cakan, M.M. Titirici, J.O. Muller, R. Schlogl, M. Antonietti, J. Maier, Angew. Chem. Int. Ed. 47 (2008) 1645–1649.
[45] L.W. Ji, Z. Lin, A.J. Medford, X.W. Zhang, Carbon 47 (2009) 3346–3354.
[46] Q. Wang, L.J. Liu, L.Q. Chen, X.J. Huang, J. Electrochem. Soc. 151 (2004) A1333–A1337.
[47] L.W. Ji, Z. Lin, A.J. Medford, X.W. Zhang, Chem. Eur. J. 15 (2009) 10718–10722.
[48] D.T. Britton, A. Hempel, M. Harting, G. Kogel, P. Sperr, W. Triftshauser, C. Arendse, D. Knoesen, Phys. Rev. B 64 (2001).
[49] G.L. Cui, Y.S. Hu, L.J. Zhi, D.Q. Wu, I. Lieberwirth, J. Maier, K. Mullen, Small 3 (2007) 2066–2069.
[50] Y.F. Shi, B.K. Guo, S.A. Corr, Q.H. Shi, Y.S. Hu, K.R. Heier, L.Q. Chen, R. Seshadri, G.D. Stucky, Nano Lett. 9 (2009) 4215–4220.
[51] L. Wang, Y. Yu, P.C. Chen, D.W. Zhang, C.H. Chen, J. Power Sources 183 (2008) 717–723.
[52] C.K. Chan, H.L. Peng, G. Liu, K. McIlwrath, X.F. Zhang, R.A. Huggins, Y. Cui, Nat. Nanotechnol. 3 (2008) 31–35.